APERTURE SYNTHESIS OBSERVATIONS OF CO, HCN, AND 89 GHz CONTINUUM EMISSION TOWARD NGC 604 IN M33: SEQUENTIAL STAR FORMATION INDUCED BY A SUPERGIANT H II REGION

Rie Miura[1,2], Sachiko K. Okumura[1,2], Tomoka Tosaki[3], Yoichi Tamura[2,4], Yasutaka Kurono[1], Nario Kuno[4],
Kouichiro Nakanishi[1], Seiichi Sakamoto[5], Takashi Hasegawa[6], and Ryohei Kawabe[4]

[1] National Astronomical Observatory of Japan, 2-21-1 Osawa, Mitaka, Tokyo 181-8588, Japan; rie.miura@nao.ac.jp
[2] Department of Astronomy, The University of Tokyo, Hongo, Bunkyo-ku, Tokyo 133-0033, Japan
[3] Joetsu University of Education, Yamayashiki-machi, Joetsu, Niigata 943-8512, Japan
[4] Nobeyama Radio Observatory, Minamimaki, Minamisaku, Nagano 384-1805, Japan
[5] Institute of Space and Astronautical Science, 3-1-1 Yoshinodai, Chuo-ku, Sagamihara-shi, Kanagawa 252-5210, Japan
[6] Gunma Astronomical Observatory, Nakayama, Takayama, Agatsuma, Gunma 377-0702, Japan

ABSTRACT

We present the results from new Nobeyama Millimeter Array observations of CO(1–0), HCN(1–0), and 89 GHz continuum emission toward NGC 604, known as the supergiant H II region in the nearby galaxy M33. Our high spatial resolution images ($4''.2 \times 2''.6$, corresponding to 17 pc × 11 pc physical size) of CO emission allowed us to uncover 10 individual molecular clouds that have masses of $(0.8–7.4) \times 10^5 \, M_\odot$ and sizes of 5–29 pc, comparable to those of typical Galactic giant molecular clouds. Moreover, we detected for the first time HCN emission in the two most massive clouds and 89 GHz continuum emission at the rims of the "Hα shells." The HCN and 89 GHz continuum emission are offset from the CO peak and are distributed in the direction of the central cluster. Three out of ten CO clouds are well correlated with the Hα shells both in spatial and velocity domains, implying an interaction between molecular gas and the expanding H II region. The CO clouds show varieties in star formation efficiencies (SFEs), which are estimated from the 89 GHz emission and combination of Hα and *Spitzer* 24 μm data. Furthermore, we found that the SFEs decrease with increasing projected distance measured from the heart of the central OB star cluster in NGC 604, suggesting radial changes in the evolutionary stages of the molecular clouds in the course of stellar cluster formation. Our results provide further support to the picture of sequential star formation in NGC 604 initially proposed by Tosaki et al. with the higher spatially resolved molecular clouds, in which an isotropic expansion of the H II region pushes gases outward, which accumulates to form dense molecular clouds, and then induces massive star formations.

Key words: galaxies: individual (M33) – H II regions – ISM: clouds – ISM: individual objects (NGC 604) – ISM: molecules – radio lines: ISM

Online-only material: color figure

1. INTRODUCTION

The expansion of an H II region can trigger star formation in various ways (see the review of Elmegreen 1998): direct compression of pre-existing clouds and globules due to the high pressure of H II regions ("globule squeezing"), and gas accumulation and cloud collapse at the edges of H II regions and supernovae remnants ("collect and collapse"). The globule squeezing process works on the smaller scale of cometary globules, while the collect and collapse process works on the larger scale of H II regions. Between these two processes, the collect and collapse process, first proposed by Elmegreen & Lada (1977), is particularly interesting as it allows the formation of massive fragments which are potential sites of massive star or cluster formation (Whitworth et al. 1994). As an H II region expands with supersonic velocity, the ambient medium is photoionized and dynamically swept up into the shocked layer, which may become gravitationally unstable and collapse to filaments, and then form dense cores in the filament. The new generation stars are formed in one or more dense cores. Many multi-wavelength studies for the collect and collapse process have been performed in our Galaxy and neighboring galaxies (see examples in Elmegreen 1998). From *JHK* photometry, stellar clusters of different ages are seen spatially resolved in an H II region, and moreover, embedded younger massive clusters are found to lie at the peripheries of H II regions (e.g., Deharveng et al. 2005, 2008; Zavagno et al. 2006). These clusters are possible second-generation clusters whose formation has been triggered by the expansion of the H II region ("propagating star formation;" Elmegreen 1998).

Mayya (1994, 1995) and Mayya & Prabhu (1996) extended this process of propagating star formation in molecular clouds to a larger scale to explain the star formation process in giant H II regions (GHRs). GHRs can easily spread over areas 10^2–10^3 pc across and play a vital role in determining the large-scale structures of their host galaxies. However, little is known about the possible connection between ambient interstellar matter and the expansion of GHRs over such distances. This is because there is no such GHR in our Galaxy, and toward external galaxies, it has been difficult to perform high-resolution, high-sensitivity, and wide-field observations all at once. Evidence of the collect and collapse process on a large scale were most notable from the correspondence between the old H I holes and young OB associations (Brinks & Bajaja 1986; Deul & den Hartog 1990), showing the kinematic and spatial evidence of expanding H I and Hα shells. Deul & den Hartog (1990) allow for the possibility that many such holes have been excavated by massive star formation activity and formed by the local collapse of H I atomic gas, giving rise to giant molecular clouds (GMCs) which are the principal sites of star formation. In fact, GMCs tend to be spatially clustered around the H I holes (Engargiola et al. 2003).

Spatially resolved studies of these GMCs are necessary in order to understand the triggers of star formation around GHRs

through the formation of dense molecular clouds which take place in individual GMCs. Recent progress in millimeter arrays provides wide-field, high-sensitivity, and high-resolution images of the molecular gas for a relatively shorter observational time, which have the potential to reveal clumps within GMCs and the physical relation to ongoing star formation. Our objective is to study how extragalactic GMCs evolve to form stars through dense gas formation which might be affected by large-scale phenomena, that is, the expansion of a GHR. In particular, we focus on the evolution of GMCs by probing their physical nature, such as their density structures and star formation activities, and their spatial distributions in a galaxy, using the multi-wavelength observations. With this purpose, we embarked on detailed studies of nearby extragalactic GMCs in a bright supergiant H II region, NGC 604.

The GHR NGC 604 is located in the northern arm of the spiral galaxy M33. The proximity (distance of 0.84 Mpc; Freedman et al. 2001) and favorable inclination of M33 ($i = 51°$; Corbelli & Salucci 2000) are sufficient to resolve gas components with little contamination along the line of sight and to understand the inner structure of GMCs (i.e., typically 40 pc in diameter; Scoville & Sanders 1987). Because of its striking features, the GHR NGC 604 has been observed in a wide range of wavelengths: radio (Viallefond et al. 1992; Wilson & Scoville 1992; Churchwell & Goss 1999; Tosaki et al. 2007), optical (Drissen et al. 1993; Hunter et al. 1996; Tenorio-Tagle et al. 2000; Maíz-Apellániz et al. 2004), and X-rays (Tüllmann et al. 2008). According to previous studies, the Hα nebula has a core–halo structure extending up to a radius of 200–400 pc (Melnick 1980, see also Figure 6). The Hα core, containing a very young (3–5 Myr) and rich (over 200) O-type stellar population, is surrounded by photoionized filaments and a section of shells (Drissen et al. 1993; Diaz et al. 1996; Hunter et al. 1996; González Delgado & Pérez 2000; Tenorio-Tagle et al. 2000; Bruhweiler et al. 2003; Relaño & Kennicutt 2009). The energy of the stellar wind has been estimated to be enough to form the core of the Hα nebula (e.g., Tenorio-Tagle et al. 2000; Maíz-Apellániz et al. 2004; Tüllmann et al. 2008); on the other hand, supernova remnants (SNRs) as well as stellar winds contribute to blow it up to the halo structure (e.g., Yang et al. 1996). As noted in Figure 6, we call the shell surrounding the main cavity "Shell A" and the shell located to the south of Shell A "Shell B," which appears to be a blowout through the molecular tunnel over Shell A (Tenorio-Tagle et al. 2000). OB and W-R stars are mostly distributed in Shell A, while a small number of OB stars are in Shell B (see Figure 7 in Yang et al. 1996). In a near-infrared *JHK* photometric study of NGC 604 recently reported in Fariña et al. (2010), the candidates of massive young stellar objects appear aligned with bright Hα Shells A and B. An H I hole surrounds a diffuse Hα nebula and some GMCs are within 150 pc around the H I hole edge (Engargiola et al. 2003; Heiner et al. 2009). The existence of five GMCs over the extent of the Hα emission in the NGC 604 region was revealed by previous ^{12}CO observations (Viallefond et al. 1992; Wilson & Scoville 1992; Engargiola et al. 2003; Rosolowsky et al. 2003). The sensitivity and spatial resolution of these observations using the OVRO interferometer and the BIMA array were, however, not sufficient to resolve the inner structure of any of these GMCs.

We present here the new results of the interferometric CO($J = 1–0$), HCN, and 89 GHz continuum observations toward the NGC 604 region. Our imaging achieved a higher spatial resolution than any other studies thus far (10 pc scale for ^{12}CO emission). We observed the $J = 1–0$ emission lines of ^{12}CO

and HCN and the adjacent 89 GHz continuum emission. These three probes trace different components of the GMC, i.e., relatively diffuse molecular clouds (the critical density of ^{12}CO line emission, $n_{H_2} \sim 10^2$ cm^{-3}), denser regions ($n_{H_2} > 10^4$ cm^{-3}), and active star-forming regions, respectively. Indeed, the HCN emission line rather than ^{12}CO has been known to trace denser regions in molecular clouds linked to star formation activities (e.g., Solomon et al. 1992). The 89 GHz continuum is considered to be mainly dominated by free–free emission from ionized gas by young OB stars, and thus expected to trace the massive star-forming region. The HCN observation and millimeter-wavelength continuum emission toward NGC 604 are reported for the first time in this work. Furthermore, this work provides the first example of extragalactic GMCs in spiral galaxies being observed on a size scale comparable to typical galactic GMCs.

The outline of this paper is as follows. The observations and data reduction are summarized in Section 2. In Section 3, the general procedure for identifying clouds in the survey and the results of each probe are described. In the discussion in Section 4, we quantify the star formation activities in the GMCs using our data and the 24 μm and Hα data, and discuss the varieties of the physical states of the identified clouds. We also discuss the relationship between the nature of these clouds and their evolutionary stage. Finally, we interpret our results in the context of a sequential star formation scenario, as initially proposed for NGC 604 by Tosaki et al. (2007) from the spatial relationship between the GMCs and Hα nebula. The summary of this work is given in Section 5.

2. OBSERVATIONS AND DATA REDUCTION

We performed ^{12}CO(1–0), HCN(1–0), and 89 GHz continuum observations toward NGC 604 using the Nobeyama Millimeter Array (NMA) at the Nobeyama Radio Observatory (NRO) from 2004 November to 2006 December. We observed the ^{12}CO line emission toward the five fields of view (FoVs) with both C and D configurations of NMA (see Figure 1, Tables 1 and 2). The area of the five FoVs was about $110'' \times 145''$, corresponding to 450 pc × 600 pc covering the entire spatial extent of the optical nebulae. The HCN(1–0) and 89 GHz continuum emission were observed toward two out of the five FoVs to cover the two largest GMCs. Toward the three other FoVs, we have not observed the HCN(1-0) and 89 GHz continuum expression, because it is expected that we need more integration time to detect them in smaller GMCs than in the two largest GMCs. The sizes of the FoVs are represented by the full width at half-maximum (FWHM) of the primary beam at each frequency and they are given in Table 2.

We used DSB SIS receivers as the front-end, and the digital spectro-correlator New-FX (1024 channels, 32 MHz bandwidth) as the back-end for the ^{12}CO and HCN observations. The total bandwidth of the FX correlator corresponds to 83.2 km s^{-1} at the ^{12}CO frequency, and to 121.6 km s^{-1} at HCN, respectively. The 89 GHz continuum observations were performed simultaneously with the HCN observations using the Ultra-Wide-Band Correlator (UWBC; Okumura et al. 2000) which has 128 channels and a bandwidth of 1024 MHz. The continuum emission data were made by merging the frequency information in the intermediate frequency signals from the lower sideband (LSB) of the UWBC. The frequency ranges containing line emissions of HCN and HCO$^+$ (89.188526 GHz) were removed from the original visibility data. The effective bandwidth of line-free channels is 768 MHz.

Table 1
^{12}CO($J = 1$–0) Observational Properties

FoV	Field Center (R.A., decl.)	Array Configuration	Integration Time (hr)	Beam Size (arcsec)	P.A. (deg)	$\sigma_{\rm rms}$[a] (MJy sr^{-1})	Flux Ratio[b]
FOV1	(01^{h}34^{m}31^s.7, +30°47′41″.0)	C,D	8.2	5.4 × 4.5	−38.1	75	0.51 ± 0.09
FOV2	(01^{h}34^{m}32^s.7, +30°47′13″.9)	C,D	7.8	5.4 × 4.5	−38.1	75	0.23 ± 0.04
FOV3	(01^{h}34^{m}33^s.3, +30°46′47″.4)	C,D	6.0	4.1 × 2.6	−46.7	147	0.62 ± 0.11
FOV4	(01^{h}34^{m}30^s.9, +30°46′53″.7)	C,D	7.9	5.4 × 4.5	−38.1	75	0.32 ± 0.06
FOV5	(01^{h}34^{m}34^s.5, +30°46′18″.4)	C,D	6.6	4.1 × 2.6	−46.7	147	0.63 ± 0.11

Notes.
[a] The rms noise was measured in the emission-free region with 1 MHz resolution on the primary-beam-corrected images. The unit was converted from Jy beam^{-1} to Jy sr^{-1} using $\Omega_{\rm beam} = \frac{\pi}{4\ln 2}\sin\theta_{\rm maj}\sin\theta_{\rm min}$, where $\Omega_{\rm beam}$ is the synthesized beam in steradians and, $\theta_{\rm maj}$ and $\theta_{\rm min}$ are the synthesized beam in arcseconds. The conversion factors are 6.5×10^{-10} sr beam^{-1} for the 5″.4 × 4″.5 resolution data, and 2.8×10^{-10} sr beam^{-1} for the 4″.1 × 2″.6 resolution data.
[b] The ratio of interferometric flux to the single dish flux (R. Miura et al. 2010, in preparation), which is measured in the box region with 42″ × 42″ at the center of each FoV.

Table 2
Observational Parameters of the Three Probes

Parameter	^{12}CO(1–0)	HCN(1–0)	89 GHz Continuum
Frequency (GHz)	115.271202	88.6304157	88.9790432 ± 0.512 (LSB)[a]
Observing period	2004 Nov–2006 Dec	2004 Nov–2006 Jan	2004 Nov–2006 Jan
Observed field	FOV1, 2, 3, 4, 5	FOV3, FOV5	FOV3, FOV5
Array configurations	C, D	C, D	C, D
Correlator	FX	FX	UWBC
Bandwidth (MHz)	32	32	1024
FWHM of FoV (″)	59	77	76
Beam size (″)	(see Table 1)	6.6 × 5.3	6.9 × 5.5
Velocity resolution (km s^{-1})	2.6	3.4	. . .
Integration time (hr)	(see Table 1)	19	19
$\sigma_{\rm rms}$ (MJy sr^{-1})[b]	(see Table 1)	21	0.6

Notes.
[a] The frequency range corresponding to the line emission as HCN and HCO+(89.188526 GHz) was removed from the original visibility data.
[b] The conversion factors are 9.3×10^{-10} sr beam^{-1} for the 6″.6 × 5″.3 resolution data, and 1.0×10^{-9} sr beam^{-1} for the 6″.9 × 5″.5 resolution data.
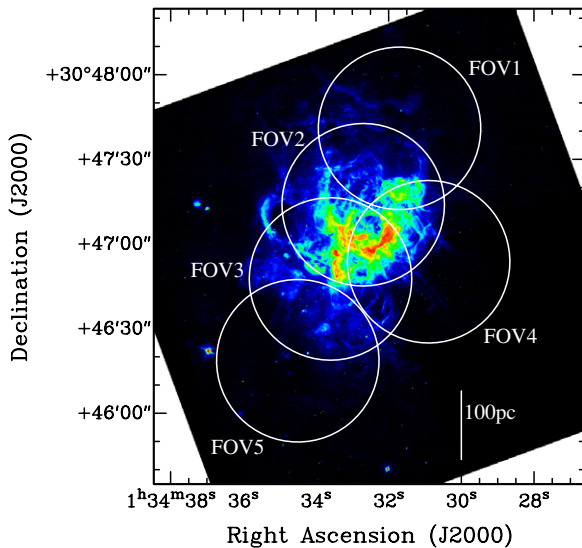
Figure 1. Positions of the five fields of view (FoVs) observed in ^{12}CO(1–0) overlaid on the distribution of Hα, which is available in the *HST* archive. The archival *HST* WFPC2 image of NGC 604 from program No. 5237 (PI: J. Westphal) is used here. Each circle corresponds to the NMA primary beam (FWHM= 59″) at 115 GHz. The field names are also labeled. The bar on the right bottom in the figure represents a linear scale of 100 pc at the distance of M33.

(A color version of this figure is available in the online journal.)

The bandpass calibration was done using the quasar 3C 454.3. The radio sources B0234+285 and B0133+476 were observed every 20 minutes as phase calibrators. The flux scales of these calibrators were determined by comparison with Uranus and Neptune. The uncertainty in the absolute flux scale is expected to be less than 15%.

The interferometric data were reduced using the NRO software package UVPROC-II (Tsutsumi et al. 1997). The final mosaicked image was made by combining the visibility data of all the available FoVs with the software package MIRIAD (using the task `invert` to make the synthesis image, and `mossdi` to CLEAN the image for the line data or `mfclean` for the continuum data). All these maps were made with natural uv weighting. The synthesized beam sizes of the ^{12}CO images for each FoV are given in Table 1, while those of the HCN and 89 GHz continuum are given in Table 2. Note that the spatial resolutions in the partially overlapped areas between the FoVs are the average of those in the overlapping FoVs.

The final three-dimensional data cube of the ^{12}CO and the HCN data has a frequency resolution of 1 MHz (corresponding to 2.6 km s^{-1} at 115 GHz, 3.4 km s^{-1} at 89 GHz, respectively) and their typical noise levels are given in Tables 1 and 2. The noise level of the 89 GHz continuum data is also given in Table 2. The noise level was measured over the emission-free area. The final flux densities and noise levels for the sources were estimated after correcting for the primary beam

attenuation. Note that the noise levels rise by a factor of 1.5 at the edges of each FoV due to the primary beam correction. Since the *uv* coverage of each pointing is not identical, the synthesized beam patterns differ among pointings. We briefly summarize the observational parameters in Tables 1 and 2 for the interferometric observations.

It is worth noting that interferometric observations are not sensitive to large-scale features (i.e., low spatial frequencies) of sizes larger than $\sim\lambda/B_{min}$, where λ is the observing wavelength and B_{min} is the minimum projected baseline. For our observations, B_{min} is 8–9 kλ at 115 GHz and 4 kλ at 89 GHz. Thus, emission structures extended over spatial scales more than $23''$–$26''$ (93–105 pc) in the 115 GHz observation, and $52''$ ($\sim$211 pc) in the 89 GHz observation, are resolved out in the interferometric images. In order to estimate the missing flux in the CO observations, we compared the total integrated fluxes for each FoV in our NMA maps to the single-dish maps obtained using the 45 m telescope at NRO (R. Miura et al. 2010, in preparation). The fluxes were measured within a $42'' \times 42''$ box at the center of each FoV. The interferometric to single-dish flux ratios are given in Column 8 of Table 1. The estimated ratios of FoV2 and FoV4 are relatively lower than the other three FoVs by less than 30% because there is little molecular gas detected in the interferometric CO observation, although the single-dish maps in FoV2 and FoV4 include the envelope of the three largest GMCs which are located at the center of FoV1, FoV3, and FoV5, respectively. The averaged ratio over the five FoVs is 0.46 ± 0.17, suggesting that half of the CO emission is resolved out in our interferometer observations.

3. RESULTS

3.1. ^{12}CO(1–0)

The CO integrated-intensity map in the velocity range $V_{LSR} = -211$ km s^{-1} to -256 km s^{-1} is shown in Figure 2. We identified CO clouds using the following criteria: cloud emission must be more than three times stronger than the rms noise level (σ_{rms}) and at least two times wider in velocity than our velocity resolution, and the cloud sizes must be larger than the equivalent area of the synthesized beam size. Ten clouds were identified with these above criteria. Their physical properties were obtained as described below.

The cloud size $\bar{D}$ is defined as the average of the deconvolved FWHM diameters in right ascension and declination. The typical error of $\bar{D}$ was estimated as an average of the spatial resolution in the individual pointings. The velocity FWHM (V_{FWHM}) was derived from Gaussian fits to the emission line. Virial masses (M_{vir}) and molecular cloud masses (M_{mol}) were calculated using the procedures described in Wilson & Scoville (1990 and references therein). They were derived using the equations, $M_{vir} = 99 D_{pc} V_{FWHM}^2 \, M_{\odot}$ and $M_{mol} = 1.61 \times 10^4 d_{Mpc}^2 S_{CO} \, M_{\odot}$, where D_{pc} is the cloud size in parsec, d_{Mpc} is the distance to M33 in Mpc, and S_{CO} is the CO flux density in Jy km s^{-1}. We used 1.4 times the deconvolved diameter of the cloud in calculating the virial mass, since this diameter was found empirically to contain most of the flux of the cloud (Wilson & Scoville 1990). Here, we assume the galactic value of the conversion factor from CO flux densities and H$_2$ column densities, $(3 \pm 1) \times 10^{20}$ cm^{-2}/ (K km s^{-1}) (Strong et al. 1988), and a factor of 1.36 has been included for the contribution of helium.

Table 3 summarizes the properties of the ten clouds we identified. The positions of the ten clouds are shown in Figure 2. The cloud sizes range from less than 5 pc to 29 pc and
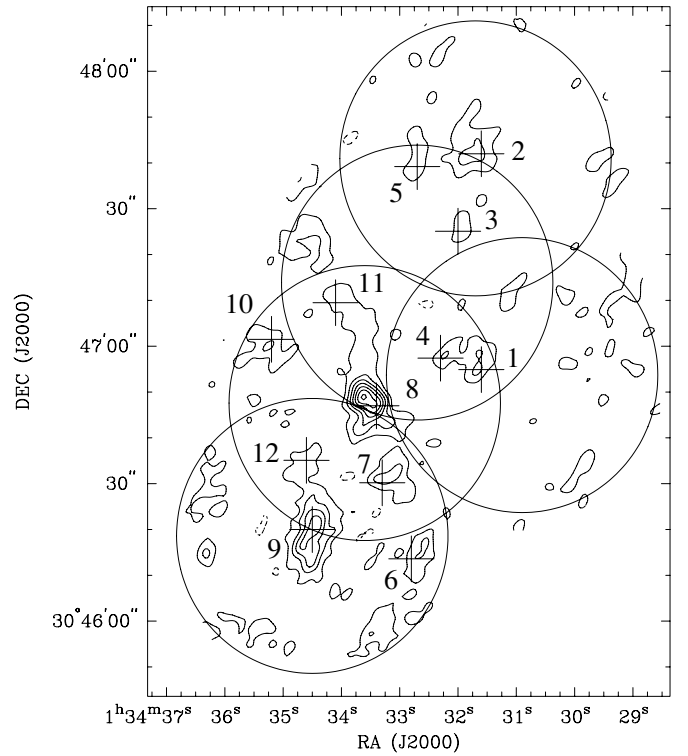
Figure 2. Total integrated-intensity map of ^{12}CO over five FoVs. Primary beam correction was applied to this image. Contour levels are $-3\sigma_{rms}$, $3\sigma_{rms}$, $6\sigma_{rms}$, $9\sigma_{rms}$, $12\sigma_{rms}$, $15\sigma_{rms}$, $18\sigma_{rms}$, and $21\sigma_{rms}$, where $1\sigma_{rms} = 1.8 \times 10^3$ MJy sr^{-1} km s^{-1}. To convert to Jy sr^{-1}, the conversion factor 2.8×10^{-10} sr beam^{-1} was used. The crosses represent the positions of the 12 identified clouds and their names are also labeled. The circles represent the five FoVs that we observed in CO line emission. The parts of the emission outside the FoVs are masked out.

their masses are in the range $(0.8$–$7.4) \times 10^5 \, M_{\odot}$, which are comparable to those of typical GMCs in the Milky Way (e.g., Scoville & Sanders 1987). Six clouds (NMA-1, NMA-3, NMA-4, NMA-5, NMA-6, and NMA-10 in Table 3) were newly identified with our observations. The rest were already reported in previous papers (Wilson & Scoville 1992; Engargiola et al. 2003).

We would like to mention two other clouds, NMA-11 and NMA-12. Even though their features do not satisfy our criteria for cloud identification, they were detected over 3σ but in only one velocity channel; they were also detected in our single dish image with the NRO 45 m telescope (R. Miura et al. 2010, in preparation). One source, NMA-11, is located to the north of NMA-8, while the other source, NMA-12, is to the north of NMA-9. The properties of these two clouds are also given in Table 3.

3.2. HCN

Two HCN emission components were marginally detected more than three times stronger than the rms noise level and over two velocity channels (each has 3.4 km s^{-1}). One is at $(01^h34^m33\overset{s}{.}4, +30°46'50\overset{''}{.}5)$ at the velocity of -245 km s^{-1} and the other at $(01^h34^m34\overset{s}{.}3, +30°46'21\overset{''}{.}0)$ at the velocity of -225 km s^{-1}. Figure 4 shows the HCN integrated-intensity map overlaid on the CO map, which were integrated over the velocity range where the emission was seen ($>3\sigma_{rms}$). These two HCN clouds seem to be associated with the CO clouds, NMA-8 and NMA-9. The peaks of both HCN clouds are offset from those of the CO clouds, and moreover, both of the HCN clouds are

Table 3
Cloud Properties for Clouds Found in M33

Cloud No.	Alternative[a] Name	$\alpha(J2000), \delta(J2000)$[b]	V_{LSR}[c] (km s^{-1})	V_{FWHM}[d] (km s^{-1})	S_{CO}[e] (Jy km s^{-1})	$\bar{D}$[f] (pc)	M_{mol} ($10^5 M_\odot$)	M_{vir} ($10^5 M_\odot$)
NMA-1		$01^h34^m31^s59, +30°46'54''88$	−241	4.9	14.4 ± 1.5	<9.4[g]	1.6	<0.3
NMA-2	EPRB-101	$01^h34^m31^s59, +30°47'42''03$	−244	10.4	22.3 ± 1.6	19.2	2.5	2.9
NMA-3		$01^h34^m31^s94, +30°47'25''14$	−250	7.3	6.6 ± 1.0	<4.9[g]	0.8	<0.4
NMA-4		$01^h34^m32^s29, +30°46'57''40$	−247	8.4	6.8 ± 1.0	10.1	0.8	1.0
NMA-5		$01^h34^m32^s74, +30°47'39''18$	−242	7.0	10.7 ± 1.7	<10.9[g]	1.2	<0.9
NMA-6		$01^h34^m32^s79, +30°46'13''55$	−240	7.9	18.4 ± 2.2	21.9	2.1	1.8
NMA-7	WS-1	$01^h34^m33^s25, +30°46'30''19$	−249	7.6	18.6 ± 1.7	19.2	2.1	1.5
NMA-8	WS-2, EPRB-8	$01^h34^m33^s42, +30°46'47''03$	−243	10.2	65.2 ± 2.7	28.9	7.4	4.1
NMA-9	WS-4, EPRB-9	$01^h34^m34^s47, +30°46'20''00$	−221	9.6	56.7 ± 2.4	27.9	6.4	3.6
NMA-10		$01^h34^m35^s16, +30°47'01''50$	−228	4.8	27.2 ± 3.2	11.0	3.1	0.4
NMA-11		$01^h34^m34^s07, +30°47'09''47$	−239	<2.6	12.4 ± 1.4	<20	1.4	<0.7
NMA-12		$01^h34^m34^s64, +30°46'35''10$	−228	<2.6	10.7 ± 1.2	<20	1.2	<0.7

Notes. The derived properties of identified clouds were described shortly in text. Approximate errors are $\delta V_{FWHM} = 1.3$ km s^{-1} (i.e., one-half the velocity resolution), $\delta M_{mol} = 38\%$, and $\delta M_{vir} = 40\%$.
[a] WS-n: from Wilson & Scoville (1992). EPRB-n: from Engargiola et al. (2003).
[b] The positions of clouds were obtained from the position of the peak of the emission.
[c] The positions along the velocity axis were obtained from the position of the peak of the observed (Gaussian-fit) LSR velocities.
[d] The full width at half-maximum velocities are deconvolved with a velocity resolution of $\delta V_{FWHM} = 1.3$ km s^{-1}.
[e] The flux densities are the corrected primary beam attenuation.
[f] $\bar{D} = D_\alpha + D_\delta$, where D_α and D_δ are the deconvolved FWHM diameters in the right ascension and declination directions. Typical error of the cloud size differs depending on where the clouds are located because the synthesized beam size differs on each FoV. Typical errors are $\delta \bar{D} = 5.1$ pc for FOV3 and FOV5, $\delta \bar{D} = 6.6$ pc for FOV1, FOV2, and FOV4.
[g] Since the cloud size in the right ascension of NMA-1, NMA-3, and NMA-5 is less than the beam size in the same direction, the cloud size $\bar{D}$ is given as the upper limit.

located on the northern side of each CO cloud, towards the center of the H II region. To check this association we have compared the velocities of the CO clouds to those of the HCN clouds. The HCN and CO spectra of these two components at the velocity resolution of 3.4 km s^{-1} are shown in Figure 3. Each spectrum was measured over the area where the emission was seen ($>3\sigma_{rms}$). The CO images were convolved to the same spatial and velocity resolution as the HCN images and the CO spectra were measured in the same region as the HCN spectra. The peak of the HCN spectra is slightly blueshifted compared to that of the CO spectra in the same spatial region, which are found in both profiles of NMA-8 and NMA-9. The bluer velocity corresponds to the downstream direction by considering the direction of galactic circular rotation (from south to north in Figure 4) in this region, and hence these two HCN components seem to be associated with the blue components of CO clouds, which are located on the downstream (northern) side.

This suggests that the components with different velocities have different flux ratios of HCN to CO. The flux ratio of HCN to CO is often used as a density probe (e.g., Helfer & Blitz 1997a). We convolved the CO images with a Gaussian function of the same beam size as that of the HCN images for comparison between the total flux densities in the CO and HCN images at the same spatial scale. We obtained each total flux density by integrating over the extent of the emission components with more than $3\sigma_{rms}$. The flux ratios of HCN to CO (S_{HCN}/S_{CO}^*[7]) were estimated to be 0.024 ± 0.007 for NMA-8 and 0.018 ± 0.007 for NMA-9. For the CO clouds where we did not detect any HCN emission (NMA-1, NMA-4, NMA-6, NMA-7, and NMA-10), we set upper limits on the line ratio using the detection limit of $3\sigma_{rms}$. The upper limits of S_{HCN}/S_{CO}^* ratios are given in Table 4.

There is a similar HCN survey of GMCs in M 31 using the IRAM 30 m radio telescope (Brouillet et al. 2005). We found that our estimates of S_{HCN}/S_{CO}^* are comparable[8] to ratios of 0.0075–0.028 that were obtained from their spectrum data of M31 at a spatial scale of ~100 pc (~28''). The S_{HCN}/S_{CO}^* ratios of the two HCN components are also comparable to those of typical galactic GMCs (0.014 ± 0.020 on average; Helfer & Blitz 1997b), which were measured in nearby GMCs at the spatial resolution of 0.5 pc.

3.3. 89 GHz Continuum

We detected the 89 GHz continuum emission in NGC 604 for the first time. Four continuum components were detected above $4\sigma_{rms}$ noise level in our synthesized image. The two strongest detections ($>5\sigma_{rms}$) in our NMA images are labeled as Source I and Source II. The right panel of Figure 5 shows the 89 GHz continuum map overlaid on the CO integrated-intensity map.

Source I was detected over $6\sigma_{rms}$ at the position ($01^h34^m33^s5$, $+30°46'55''9$) and appears to be associated with NMA-8 (within 9''). Source II was detected over $5\sigma_{rms}$ at the position ($01^h34^m32^s1$, $+30°46'59''3$) which is consistent with the position of the CO emission peak of NMA-4. Thus, we consider that these two 89 GHz components can be physically associated with NMA-8 and NMA-4, respectively. Moreover, we found that the distribution of these sources, Source I and Source II, exhibits a similarity to the 8.4 GHz continuum emission components A–D presented in Churchwell & Goss (1999); our Source I corresponds to the position of their A and B components, while our Source II corresponds to the position of their C and D components (see Figure 5). The other two components, Source III and Source IV, are located at ($01^h34^m32^s4$, $+30°47'18''8$) and

---

[7] We define the CO flux densities in the convolved images as S_{CO}^*.

[8] This might infer that the missing fluxes in our interferometric observations are nearly equal between the CO images and the HCN images.
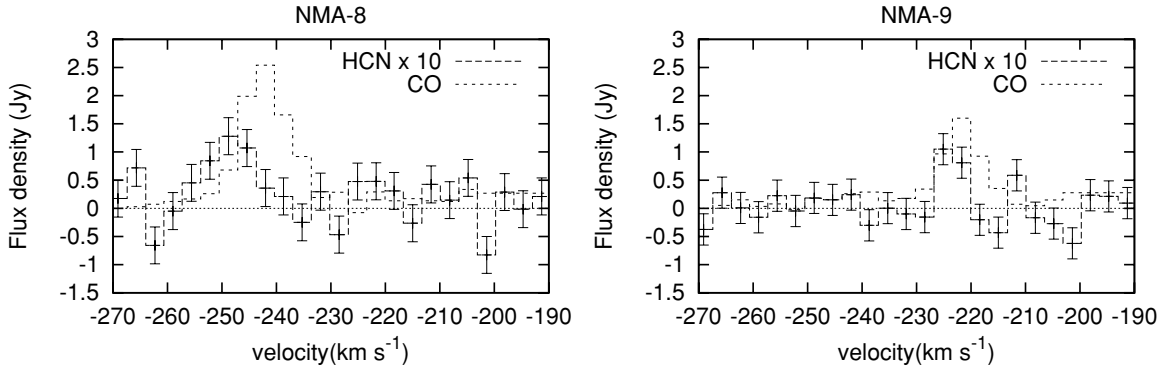
Figure 3. Spectra of the two HCN components. The left panel is one component associated with the CO molecular cloud NMA-8, while the right panel is the other associated with NMA-9. The CO spectra for NMA-8 and NMA-9, which are measured in the same region on the convolved image with the same synthesized beam and with the same velocity resolution as the HCN image, are also shown.
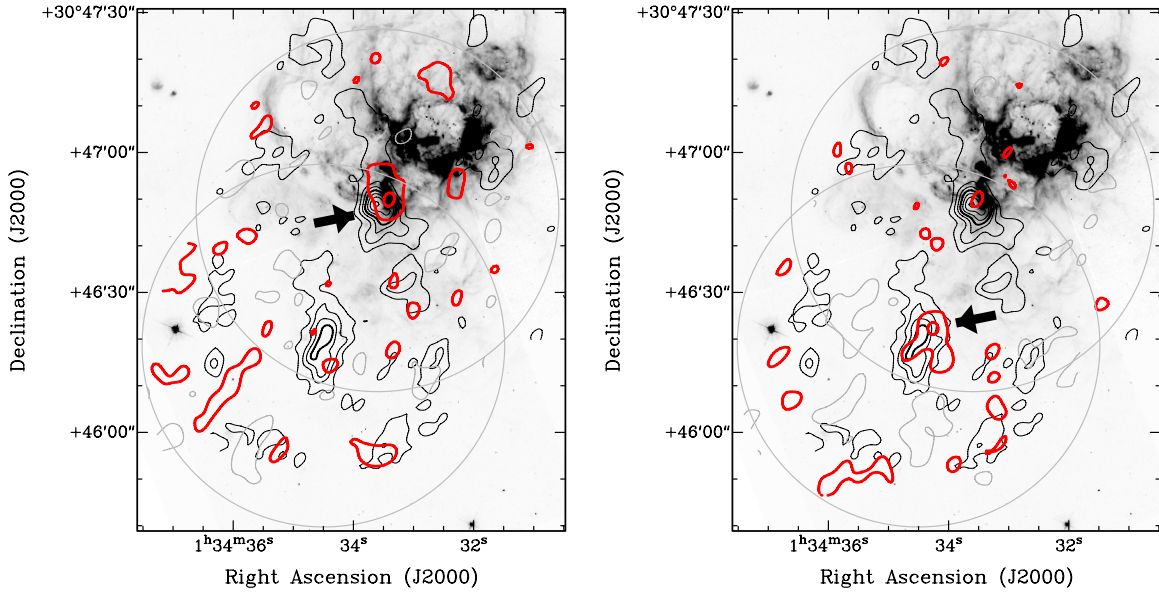
Figure 4. Total integrated-intensity map of HCN (red contours) and CO (black contour) overlaid on the Hα image (gray scale) for NMA-8 (left) and NMA-9 (right). The integrated velocity ranges are from $V_{LSR} = -245$ km s^{-1} to -252 km s^{-1} for NMA-8, and from $V_{LSR} = -222$ km s^{-1} to -225 km s^{-1} for NMA-9. The contour levels for the HCN map are $-2.5\sigma_{rms}$, $2.5\sigma_{rms}$, $5\sigma_{rms}$, where $1\sigma_{rms} = 1.5 \times 10^2$ MJy sr^{-1} km s^{-1}. The conversion factor from Jy beam^{-1} to Jy sr^{-1} is 9.3×10^{-10} sr beam^{-1} for the $6\farcs6 \times 5\farcs3$ resolution data. The negative contours are drawn as gray contour. The black contour levels for CO are $3\sigma_{rms}$, $6\sigma_{rms}$, $9\sigma_{rms}$, $12\sigma_{rms}$, $15\sigma_{rms}$, $18\sigma_{rms}$, and $21\sigma_{rms}$. The gray circles with diameter of $77''$ are the two FoVs that we observed in HCN and 89 GHz continuum emission. The black arrows indicate the region where HCN emission was detected over two channels and with $>3\sigma$. The parts of the emission outside the FoVs are masked out. Primary beam correction was applied to these images.

(01^{h}34^{m}32^s.8, +30°46′28″.8), respectively. The signal-to-noise ratio of these components is low ($<5\sigma_{rms}$) and Source III is located at the edge of the FoV. In addition, neither the CO clouds nor the 8.4 GHz emissions are found to be associated with them. Therefore, we do not consider Sources III and IV in further discussions.

We measured the flux densities over the region where the emission was seen ($>3\sigma_{rms}$) and the errors of the total flux densities were estimated by taking into account the uncertainties in the absolute flux scale and the noise fluctuations. The estimated flux densities of the two components are 3.4 ± 0.9 mJy and 9.1 ± 1.5 mJy in the NMA-4 region (Source II) and in the NMA-8 region (Source I), respectively. The millimeter-wavelength continuum flux provides a constraint on the emission measure of ionized gas, from which we can obtain information about the number of stars present for models of the number of UV photons. This is because the free–free emission from the gas ionized by OB stars contributes largely to millimeter wavelengths and is optically thin at millimeter wavelengths. Other contributions to

millimeter wavelength continuum, non-thermal radiation from SNRs, and thermal emission from interstellar dust, are expected to be small. Assuming that the 89 GHz continuum flux densities are entirely dominated by free–free emission from the ionized gas, we calculated the total production rate of ionizing photons from the observed 89 GHz continuum flux densities.

In the calculation, we followed Equation (2) in Scoville et al. (1991), which provides the relationship of the free–free emission flux density at 110 GHz to the total production rate of ionizing photons for optically thin plasma. Using the thermal (free–free) spectral index of -0.1 in M33 (Buczilowski 1988), the relationship of the free–free emission flux density at 89 GHz ($S_{89\,GHz}$) and the total production rate of ionizing photons (Q^*s^{-1}) is given by:

$$S_{89\,GHz} = 8.58 \times 10^{-2} \frac{Q^*/10^{49}\text{s}^{-1}}{d^2_{Mpc}} \text{ mJy}, \qquad (1)$$

where d_{Mpc} is the distance to M33. The H II regions are assumed
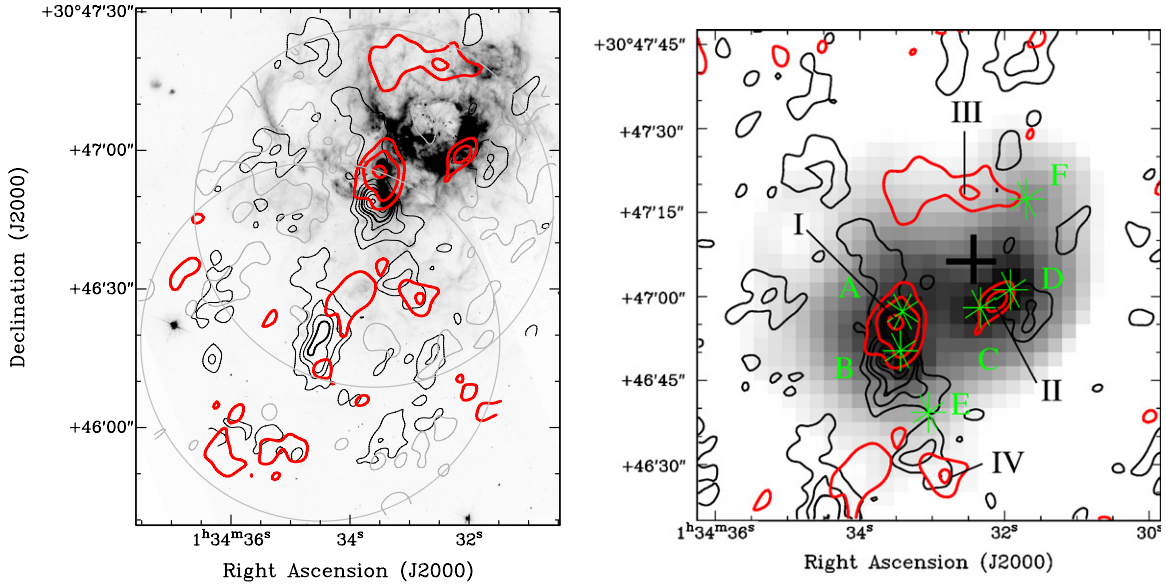
Figure 5. Left: 89 GHz continuum map (red contour) and CO (black contour) overlaid on the Hα (gray scale). The red contour levels for the 89 GHz continuum map are $-2\sigma_{rms}$, $2\sigma_{rms}$, $4\sigma_{rms}$, and $6\sigma_{rms}$, where $1\sigma_{rms} = 0.6\,\mathrm{MJy\,sr^{-1}}$, corresponding to 0.6 mJy beam^{-1} for the $6''.9 \times 5''.5$ resolution data. The negative contours are drawn in gray. The black contour levels for CO are $3\sigma_{rms}$, $6\sigma_{rms}$, $9\sigma_{rms}$, $12\sigma_{rms}$, $15\sigma_{rms}$, $18\sigma_{rms}$, and $21\sigma_{rms}$. The gray circles with diameter of $77''$ are the two FoVs that we observed in HCN and 89 GHz continuum emission. The parts of the emission outside the FoVs are masked out. Primary beam correction was applied to this image. Right: comparison of the 89 GHz continuum emission (red contour) with the 24 μm emission (gray scale) overlaid on the CO image (black contour). The 89 GHz source names (I–IV) are labeled. The cross symbol indicates the position of the center of the main cavity in NGC 604. The green star symbols represent the peak position of the 8.4 GHz components (A–F) by Churchwell & Goss (1999).

Table 4
Cloud Properties and Star Formation Activities for Clouds

Cloud No.	d_c[a] (pc)	S_{HCN}[b] (Jy km s^{-1})	S_{HCN}/S_{CO}^*[c] (10^{-2})	$S_{89\,GHz}$[b] (mJy)	SFE$_{89\,GHz}$[d] (%)	log L_{corr}(Hα)[e] (erg s^{-1})	SFE$_{Hα,24\,\mu m}$[f] (%)
NMA-1	86	. . .	. . .	<2.6	<5.0	38.58	6.2 ± 3.3
NMA-2	214	. . .	. . .	. . .	. . .	37.53	0.4 ± 0.2
NMA-3	120	. . .	. . .	. . .	. . .	37.78	2.5 ± 1.3
NMA-4	35	. . .	. . .	3.4 ± 0.9	12.4 ± 6.6	38.75	17.2 ± 9.3
NMA-5	152	. . .	. . .	. . .	. . .	37.64	1.1 ± 0.6
NMA-6	246	<0.3	<2.8	<2.1	<3.1	37.32	0.3 ± 0.2
NMA-7	194	<0.3	<2.7	<1.8	<3.6	37.96	1.6 ± 0.8
NMA-8	138	1.1 ± 0.3	2.4 ± 0.7	9.1 ± 1.5	5.1 ± 2.3	39.08	5.9 ± 3.0
NMA-9	320	0.6 ± 0.2	1.8 ± 0.7	<1.8	<1.2	37.67	0.3 ± 0.1
NMA-10	261	<0.4	<2.8	<2.3	<2.3	38.08	1.1 ± 0.6
NMA-1,4	60	<0.4	<3.2	. . .	. . .	. . .	. . .

Notes.

[a] The projected distance from the central cluster, d_c, is given in parsec relative to (01^{h}34^{m}32^s.4, +30°47′00″.3).

[b] For the clouds where no HCN emission was detected, the upper limits of the line ratio are given by using the detection limit of $3\sigma_{rms}$.

[c] The CO flux densities, S_{CO}^*, were measured over the extent of CO emissions (>$3\sigma_{rms}$) on the convolved images with HCN synthesized beam.

[d] The SFE$_{89\,GHz}$ was obtained using the following equation, SFE$_{89\,GHz} = M_{star}/(M_{star} + M_{mol}^*)$, where M_{mol}^* represents the missing-flux-corrected molecular masses. See details in the text.

[e] The extinction-corrected Hα luminosity is defined as a linear combination of these two luminosities: $L_{corr}(Hα) = L_{obs}(Hα) + a \times L(24\,\mu m)$, where $a = (0.031 \pm 0.006)$ (Calzetti et al. 2007). $\delta L_{corr}(Hα) \sim 28\%$.

[f] The SFE$_{Hα,24\,\mu m}$ was obtained using the same equation as SFE$_{89\,GHz}$. See details in the text.

to be ionization-bounded at a temperature of 10^4 K. The total production rates of ionizing photons are $(28.0 \pm 7.3) \times 10^{49}$ s^{-1} in the NMA-4 region (Source II) and $(74.8 \pm 12.3) \times 10^{49}$ s^{-1} in the NMA-8 region (Source I). The value for Source I is consistent with the total value expected from the 8.4 GHz fluxes of components A and B (68×10^{49} s^{-1}; Churchwell & Goss 1999). As for Source II, it is not consistent with the C and D components (64×10^{49} s^{-1}). It is possible that more flux from large-scale structures in NMA-4 are resolved out than those in NMA-8, because the missing flux in interferometric

observations depends on the sizes of the emission sources. Assuming that the missing flux at the 89 GHz continuum is the same as that of the CO images, the ionizing photon production rate for the NMA-4 region is consistent with that from the 8.4 GHz fluxes of components C and D.

3.4. Overall Features and Comparison with Hα

In this section, we compare the distributions of CO, HCN, and 89 GHz continuum emissions with the morphology of the Hα
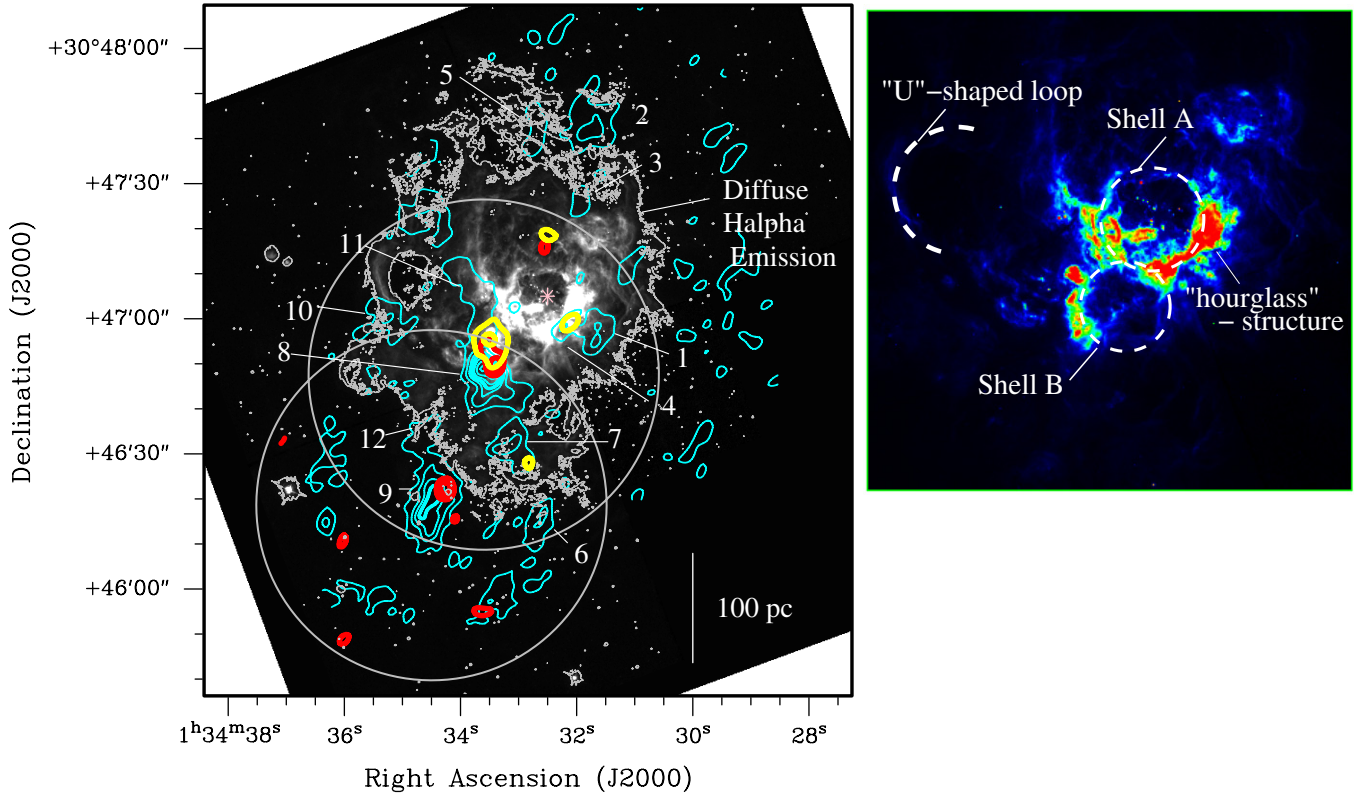
Figure 6. Left: interferometric integrated-intensity maps of ^{12}CO($J = 1$–0) emission (cyan), HCN emission (red), and 89 GHz continuum (yellow) overlaid on a color image of Hα (gray scale) by *HST*—the same images as in Figures 1–5. However, yellow contour levels are $> 4\sigma_{rms}$ and red contour levels are $4\sigma_{rms}$, $5\sigma_{rms}$ in order to show clearly the peak positions. The gray contour levels are 0.2% of the peak intensity so as to show the extent of the diffuse Hα emission nebula. The pink star symbol indicates the position of the center of the main cavity in NGC 604. The gray circles with diameter of $77''$ are the two FoVs that we observed in HCN and 89 GHz continuum emission. The cloud numbers and linear scale bar are also plotted. Right: the trimmed image of Figure 1 shows the features of the main shells and annotations discussed in the text. The locations of two shells A and B are indicated on the map.

shells in NGC 604. The composite image of CO and HCN line emissions, and the 89 GHz continuum emission overlaid onto the Hα image obtained by the *Hubble Space Telescope* (*HST*), is shown in Figure 6.

Three out of the ten identified clouds (and NMA-11) are associated with bright shells, i.e., Shell A and Shell B (see Figure 6). The bright western part of Shell A shows an hourglass-like structure, which appears to be fitted by the distribution of the ^{12}CO emission of NMA-4. The velocity structures of these Hα shells show true expansion (Yang et al. 1996), possibly powered by stellar winds from the central OB star clusters and/or SNRs (Section 1). The line-of-sight velocity of NMA-4 (-247 km s^{-1}) corresponds to that of the Hα shell at the same position (Hα emission reported in Tenorio-Tagle et al. 2000), which is Shell A. Therefore, it is considered that NMA-4 is a cloud component associated with the expanding Hα shell, Shell A. The cloud NMA-11, the marginally detected cloud, is also located on the eastern part of Shell A.

The cloud NMA-8 itself has an arc-like structure and is distributed to surround the cavity, nicely tracing the bright rim of Shell B. The 89 GHz continuum and HCN emission, which are considered to be associated with NMA-8, were detected in the inner wall of Shell B, i.e., in the direction of the central stellar cluster. Moreover, there is an offset between the peak positions of the three probes: CO, HCN, and 89 GHz continuum emissions, which are aligned to the direction of central stellar clusters (from south to north). The line-of-sight velocity of NMA-8 (-243 km s^{-1}) corresponds to that of the Hα shell at this position (Tenorio-Tagle et al. 2000), which is Shell B.

Therefore, it is considered that NMA-8 is a cloud component associated with the expanding shell B.

Looking toward the halo structure of the Hα nebula, the distribution of the ^{12}CO emission of NMA-2, NMA-6, NMA-9, and NMA-12 does not overlap with the area seen in the Hα emission but extend along the edge of diffuse Hα emission. Although it is difficult to address whether or not they are physically associated with the diffuse Hα emission due to lack of spectral data of Hα, we would like to mention an interesting feature of the dense-gas-forming region: the HCN component detected around the NMA-9 cloud, showing an offset between the CO peak and HCN peak, is located in the northern part of NMA-9; i.e., in the direction of the Hα nebula. As for the rest of the clouds, they are seen on the diffuse Hα emission. The cloud NMA-10 is located in the southern part of the "U"-shaped Hα loop, which marginally shows expansion signatures (Tenorio-Tagle et al. 2000).

Consequently, we found the distribution of CO, HCN, and 89 GHz continuum emissions which we detected in our observations are well correlated with the expanding Hα shells in NGC 604, in both morphology and kinematics. In contrast with the concentration of molecular gas on the rim of shells, no molecular clouds are observed inside Shells A and B.

4. DISCUSSION

4.1. Comparison with 24 μm and Hα Emission

In this section, we derive the star formation efficiencies (SFEs) from available *Spitzer* Archival 24 μm data and Hα

data in order to discuss the star formation activities over all five FoVs, because a combination of Hα and 24 μm luminosities is a better tracer of the total star formation rate (SFR; Kennicutt et al. 2007). We then compared the SFEs with those inferred from our 89 GHz data.

The 24 μm emission is often used as an indicator of current star formation because it is radiated from dust grains heated by newly formed massive stars (e.g., Relaño & Kennicutt 2009). The Hα emission is also directly linked to star formation; however, it is only sensitive to the ionizing photons unabsorbed by dust. A linear combination of the 24 μm emission, tracing the obscured star formation, and the observed Hα luminosity, tracing the unabsorbed star formation, which correlates better than other SFR tracers with the extinction-corrected Hα luminosity, is empirically known (Calzetti et al. 2007).

We retrieved the 24 μm images of M33 obtained with MIPS (Rieke et al. 2004) from the *Spitzer Space Telescope* (Werner et al. 2004) data archive. The basic calibrated data were created using the *Spitzer* Science Center pipeline. Background matching was applied between overlapping FoVs and background gradient was removed. The FWHM of the point-spread function in the image is 5″.7 and the grid size of the final image is 2″.5 pixel^{-1}. Our 89 GHz continuum image was overlaid on the resultant 24 μm image as shown in Figure 5. Both Source I and Source II in our 89 GHz continuum image correspond to peaks in the 24 μm map. This is one of the evidence that the 24 μm and the 89 GHz continuum emission both trace sites of star formation embedded in dust clouds.

The reduced data of Hα emission in M33 were kindly provided by R. Walterbos. It was observed with the 0.6 m Burrell–Schmidt telescope at Kitt Peak National Observatory. The dimensions of the CCD are 2048 × 2048 with pixels of 2″.03 and a total FoV of about 70′ × 70′, and then trimmed to the same size of our CO image in NGC 604. The sensitivity is 0.8×10^{17} erg s^{-1} cm^{-2} arcsec^{-2} (Hoopes et al. 2001). More details of the observations and reduction process are described in Hoopes & Walterbos (2000).

4.1.1. SFE from 89 GHz Continuum Emission

The total stellar mass can be compared with the mass of the molecular clouds to measure SFE. The SFE$_{89\,GHz}$ is defined as follows:

$$\mathrm{SFE}_{89\,\mathrm{GHz}} = \frac{M_{\mathrm{star}}}{M_{\mathrm{star}} + M^*_{\mathrm{mol}}}, \qquad (2)$$

where $M_{\mathrm{star}} = \int_{M_{\mathrm{min}}}^{M_{\mathrm{max}}} N(M) M \, dM$ is total stellar mass between M_{min} and M_{max}, and $N(M)$ represents the stellar mass function. We defined the missing-flux-corrected molecular cloud mass as M^*_{mol} using the missing flux derived in Section 2. We analyzed the total number of stars from the total ionizing photon rates (Section 3.3) using the ionizing rates of each O-type star (O9.5 v–O3 v; Martins et al. 2005), because these stellar spectral types are considered to be largely responsible for the ionizing photons of interstellar matter. We assumed that the H II regions in NGC 604 have Salpeter initial mass functions (IMFs, 2.35; González Delgado & Pérez 2000) with mass limits of 0.1–58 $M_\odot$ (corresponding up to spectral type O3 v; Martins et al. 2005). The number of O-type stars (O9.5 v–O3 v) in the NMA-4 and NMA-8 region is 185 ± 31 and 70 ± 18 stars, respectively. The SFE$_{89\,GHz}$ was estimated to be 12.4% ± 6.6% for NMA-4 and 5.1% ± 2.3% for NMA-8. As for other clouds which were not detected in continuum emission, upper limits of SFE$_{89\,GHz}$ were calculated and they are given in Table 4.

4.1.2. SFE from 24 μm Emission and Hα Emission

The Hα and 24 μm images were convolved into a common 5″.7 resolution and regridded to 2″.5 pixel^{-1}. We measured the 24 μm and Hα luminosities over the same spatial regions of all the CO clouds we identified. We measured the integrated flux over the extent of the Hα nebula and compared it with previously reported fluxes from the literature (Kennicutt 1984). The Hα fluxes in Relaño & Kennicutt (2009) are computed from the observed Hα+[N II] fluxes using the spectroscopically determined [N II]/Hα ratios (Bosch et al. 2002). The extinction-corrected Hα luminosity is then expressed as a linear combination of these two luminosities: $L_{\mathrm{corr}}(\mathrm{H}\alpha) = L_{\mathrm{obs}}(\mathrm{H}\alpha) + a \times L(24\,\mu\mathrm{m})$, where $a = (0.031 \pm 0.006)$ (Calzetti et al. 2007). Ionizing photon rates are derived from extinction-corrected Hα luminosities $L(\mathrm{H}\alpha_{\mathrm{corr}})$ using

$$Q^*(s^{-1}) = 7.32 \times 10^{11} L_{\mathrm{corr}}(\mathrm{H}\alpha)\,(\mathrm{erg\,s^{-1}}), \qquad (3)$$

which assumes an ionization bounded case B nebula (Mayya & Prabhu 1996, and references therein). The SFE from 24 μm and Hα (SFE$_{\mathrm{H}\alpha,24\,\mu\mathrm{m}}$) was calculated using the same procedures described in Section 4.1.1. The SFE$_{\mathrm{H}\alpha,24\,\mu\mathrm{m}}$ for each cloud is given in Table 4. The NMA-4 has the highest SFE of all clouds and there is the same tendency in both SFEs. The derived SFE$_{\mathrm{H}\alpha,24\,\mu\mathrm{m}}$ of 0.2%–11.5% is in good agreement with that from the 89 GHz continuum (<1.2%–12.4%) within errors.

The total amount of the ionizing photon rate (Q^*) in the NGC 604 region as a whole (within a radius of 400 pc) is 413 photons s^{-1}. The summation of Q^* over the identified clouds is 188×10^{49} photons s^{-1}, which occupies about 46% of the total Q^* of the whole region. On the other hand, the Q^* from the central stellar clusters (∼200 O stars) is estimated to be 145×10^{49} photons s^{-1}, assuming that the central stellar clusters have Salpeter IMF (2.35) and Martins et al.'s (2005) ionizing photon rates for each stellar spectral type, which contributes about 35% to the total Q^* of a whole region. Thus, this implies that such a large ionized region has been created not only by the central stellar cluster but also by the embedded stellar clusters in the clouds.

4.1.3. Comparison to Other H II Regions

In comparison, we derive the SFEs of three well-known H II regions (Orion A, W49A, and 30 Doradus) in the Local Group. The first two H II regions contain similar molecular cloud mass (i.e., mass of $1–7 \times 10^5 M_\odot$) to our identified CO clouds in NGC 604. Orion A is the nearest and most well-studied region of star formation in our Galaxy, and is known to be excited by a few late O-type stars or early B-type stars (e.g., Cardelli & Clayton 1988). W49A is one of the most massive and luminous H II regions in our Galaxy and contains 30 individual ultracompact H II regions, corresponding to about that number of OB stars (Conti & Blum 2002). The most luminous in the Large Magellanic Cloud, the 30 Doradus GHR, is introduced to compare with the secondary luminous H II region, NGC 604. Very luminous NGC 604-class H II regions are absent in our Galaxy, and hence it is frequently compared to the NGC 604, although 30 Doradus has about 3–4 times the total ionizing flux as NGC 604. The estimated SFEs obtained with the same assumptions above are tabulated in Table 5. The Q^* of Orion A was determined from the stellar types in Cardelli & Clayton (1988) and the SFE of Orion A is 2.2%. The Q^* of W49A was calculated from the measurement of combining the 25 μm luminosity (Ward-Thompson & Robson 1990) and Hα emission

Table 5
Star Formation Efficiencies of Nearby H II Regions

Cloud	Mass ($10^5\ M_\odot$)	Q^* (10^{49} s^{-1})	SFE	References
Orion A	1	2.7[a]	2.2	1
W49A	7	182	18.2	1, 2, 3
30 Doradus	9[b]	1122[c]	52.8	2, 4
NGC 604	51[d]	478[e]	7.4	This work
...NMA-4	2[d]	28	12.5	This work
...NMA-8	12[d]	75	5.1	This work

Notes. The SFE was calculated assuming the same IMF (2.35) throughout all regions. The typical error of the SFE is $\sim$50%.
[a] The ionizing photon rates in Orion A is determined from the stellar types in Cardelli & Clayton (1988).
[b] This value is the summation of the molecular cloud mass of GMCs which are annotated by 183, 186, and 189 in Fukui et al. (2008), and which are located within the extent of Hα emission in 30 Doradus ($\sim$370 pc; Kennicutt 1984).
[c] The ionizing photon rate Q^* is derived only from Hα luminosities (Kennicutt 1984), and hence the SFE can give the lower limit.
[d] They represent the missing-flux-corrected molecular masses ($M^*_{\rm mol}$).
[e] The ionizing photon rate Q^* is derived from the extinction-corrected Hα luminosities measured over a whole extent of Hα.
References. (1) Williams & McKee 1997, and references therein; (2) Kennicutt 1984; (3) Ward-Thompson & Robson 1990; (4) Fukui et al. 2008.

(Kennicutt 1984), and this can be a value of 182×10^{49} s^{-1}. The Q^* of 30 Doradus is derived only from Hα emission (Kennicutt 1984), and thus the SFE of 30 Doradus can be more than 52.8%. The SFE of NMA-4 is much larger than Orion A and comparable to those of the galactic H II region W49A, while the SFE of NMA-8 is comparable to or slightly less than W49A. The SFE of each decomposed cloud in the supergiant H II region NGC 604 is quite similar to that of the galactic H II region. Both NMA-4 and NMA-8 have about 3–10 times lower SFEs than 30 Doradus, although they need to be compared on the same scale.

The average efficiency of star formation out of giant molecular associations (e.g., Rand & Kulkarni 1990) in other extragalactic GHRs tends to be about 1%–10% out of the parental molecular cloud mass (10^6–$10^7\ M_\odot$, Mayya & Prabhu 1996). In order to compare their SFEs with that of NGC 604 on the same scale, the total (missing-flux-corrected) mass in the NGC 604 region is estimated to be $51 \times 10^5\ M_\odot$, and the extinction-corrected Hα luminosities $L_{\rm corr}$(Hα) is estimated to be 4.3×10^{39} s^{-1}. The derived SFE over the NGC 604 region is 7%. This is in good agreement with that of other extragalactic GHRs. On the other hand, the SFE of the most luminous H II region 30 Doradus is extremely higher than NGC 604 or any other GHRs, which suggests that half of its parental molecular clouds have been converted into stars and also that dozens of O-stars would have dissipated a whole GMC. NGC 604 may have the potential to continue star formation activity, which leads to a 30 Doradus-scale GHR, since NGC 604 still contains a considerable reservoir of molecular gas to be used for star formation.

4.2. The Different Properties and Evolution of GMCs

As we mentioned in the previous section, we found that the identified clouds have different SFEs (see Table 4). Specifically, NMA-4, NMA-8, and NMA-9 have conspicuous differences in their SFE$_{{\rm H}\alpha, 24\,\mu{\rm m}}$. In this section, we focus on these clouds and discuss the relationship between their different properties and their evolutionary stages.

4.2.1. NMA-4 and NMA-8

NMA-4 is located near the central stellar clusters (the projected distance from the clusters is $\sim$32 pc) and also along the bright rim of Shell A (western part of Shell A; see also Figure 6). The cavity surrounded by Shell A is known to be filled with hot coronal gas that emits X-rays and is transparent to the ionizing UV (Maíz-Apellániz et al. 2004; Tüllmann et al. 2008). The 8 μm emission, which is often used as tracer of photo-dissociation regions, is mostly distributed around the UV emission (see Figure 2 in Relaño & Kennicutt 2009), where the clouds NMA-8 and NMA-4 are located. NMA-4 and part of NMA-8 are considered to be directly exposed to the UV radiation from young massive stars.

In comparing the physical properties of NMA-4 with NMA-8, we found enough significant differences to distinguish between their evolutionary stages. The clouds NMA-4 and NMA-8 have the highest SFE and the second-highest SFE, respectively, and nevertheless, their SFEs are different by a factor of $\sim$3. The significant difference in SFEs is mainly due to the respective masses of their molecular gas; NMA-4 has a cloud mass of $\sim0.8 \times 10^5\ M_\odot$ and size of $\sim$10 pc, while NMA-8 has a cloud mass of $\sim7.4 \times 10^5\ M_\odot$ and size of $\sim$29 pc. These results might suggest that most of the cloud mass in NMA-4 has been more affected by star formation activities, i.e., conversion into stars, dissipation by stellar winds, or disruption by intensive photo-dissociation, than in NMA-8. The cloud NMA-8 is one of the largest molecular clouds and shows obvious signs of dense gas formation (Section 3.2). Since NMA-8 still contains a considerable reservoir of molecular gas and the dense gas that has not yet been dissipated by UV radiation, it is likely to undergo star formation activities. The cloud NMA-8 could be at a stage of ongoing massive star formation as well as dense gas formation.

4.2.2. NMA-9

This is the second largest cloud (size of $\sim$28 pc and mass of $\sim6.4 \times 10^5\ M_\odot$) with the lowest SFE. Its low SFE$_{24\,\mu{\rm m}}$ suggests

a lack of recent massive star formation. This cloud includes dense molecular gas, which is suggested by the detection of HCN line emission. Therefore, NMA-9 might be just forming dense molecular gas in the GMC but not be forming stars yet.

4.2.3. The Other Clouds

The other clouds show much lower values in $SFE_{24\,\mu m}$ than NMA-8 and NMA-4. We are not sure whether they include dense gas or not because HCN emissions were not detected over $3\sigma_{rms}$ in some clouds (NMA-1, NMA-6, NMA-7, and NMA-10). The S_{HCN}/S_{CO}^* ratio upper limits allow for the possibility that CO clouds have dense gas fractions similar to typical GMCs (Helfer & Blitz 1997b; Brouillet et al. 2005). Much deeper HCN observations are necessary to distinguish different properties from the dense gas fraction. Even though the other clouds (NMA-2, NMA-3, and NMA-5) have not been observed in HCN emission, we briefly describe the possibility of dense gas formation in the third largest cloud, NMA-2, since CO(3–2) emission was detected (Tosaki et al. 2007). CO(3–2) is often used as a tracer of warmer and/or denser molecular gas ($n_{H_2} \sim 10^4$ cm^{-3}, $T_{crit} = 33$ K) over CO(1–0). In fact, CO(3–2) is a better tracer of density than temperature in the region where the CO(3–2)/CO(1–0) ratio is less than 0.7, assuming the kinetic temperature is low ($\sim$20 K; Muraoka et al. 2007). Its CO(3–2)/CO(1–0) ratio ($\sim$0.5) has a value similar to that of the second largest cloud NMA-9 (Tosaki et al. 2007). Since NMA-9 shows no sign of star formation but only dense gas formation in our results, the detection of CO(3–2) emission from this cloud could be due to the dense gas formation rather than heating by embedded young stars. Considering that NMA-2 has low $SFE_{H\alpha,24\,\mu m}$ and shows little sign of star formation, NMA-2 is likely to have a similar status regarding dense gas and star formation, i.e., the clouds include a significant fraction of dense gas but have low star formation activities.

In summary, NMA-9, NMA-8, and NMA-4 seem to have significantly different properties in terms of dense gas formation and massive star formation. This variation can be explained as differences in their evolutionary stages, from dense gas formation to star formation. Cloud NMA-9 could be at the stage of "dense gas formation with no massive star formation." Cloud NMA-8 could be at a more evolved stage of "dense gas and ongoing massive star formation" than NMA-9. Cloud NMA-4 could be at the most evolved stage of "remnant" cloud where most of the molecular gas has already been converted into stars and has been dispersed by newly born massive stars.

4.3. Sequential Star Formation in NGC 604

As we mentioned in the previous section, we found a distinct difference in the physical states of star formation among the GMCs in the NGC 604 region and explained it as a difference in their evolutionary stages. Furthermore, these GMCs are well correlated with the spatial structure, and some of them also with the kinematics, of the Hα nebula including the expanding shells (Section 3.4). The physical properties and the evolution of GMCs are straightforwardly expected to be affected by the H II region excited by the stellar activities of OB clusters. Shell B might have been formed by the blowout through the molecular tunnel over Shell A (Tenorio-Tagle et al. 2000) and is estimated to be younger than Shell A (Yang et al. 1996), which is in good agreement with the fact that NMA-8 is at a younger stage than NMA-4 because NMA-4 already has dissipated parent molecular cloud (Section 4.2). These results are explained with
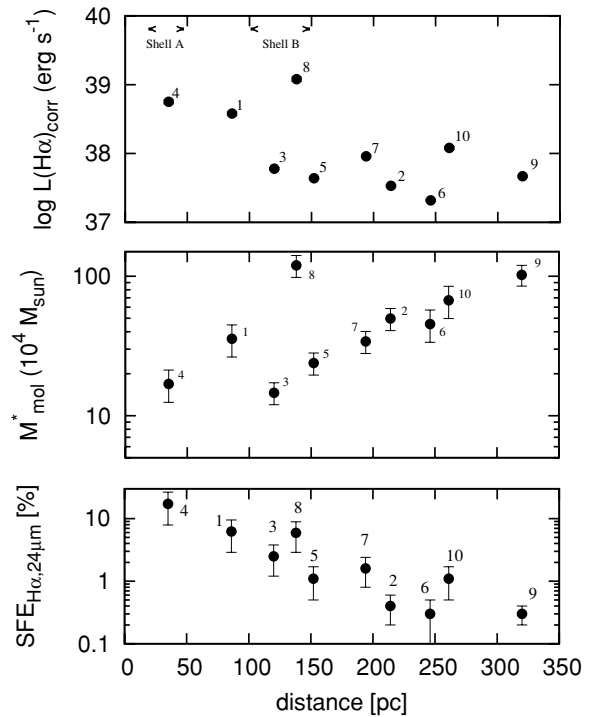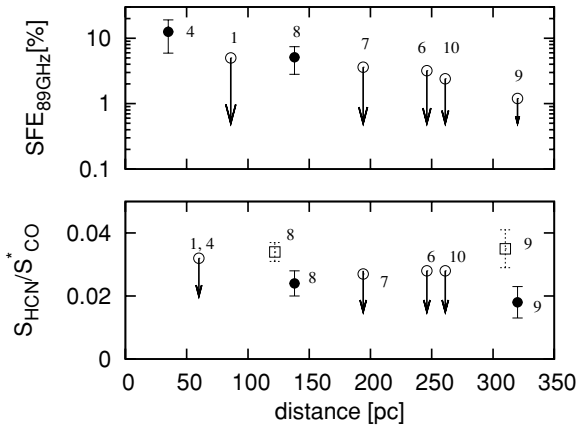

Figure 7. $L(H\alpha)_{corr}$ (top), M_{mol}^* (middle), and $SFE_{H\alpha,24\,\mu m}$ (top) distribution as a function of projected distance from the center of the main cavity in NGC 604. Its coordinate of (01^{h}34^{m}32^s.5, +30°47′0″.5) is indicated by a pink star symbol in Figure 6. The cloud numbers are also plotted. In the top panel, the locations of the two Hα shells are indicated for reference. Note that common errors are excluded in order to compare each cloud relatively.

the scenario of sequential star formation in NGC 604 that was previously proposed (Tosaki et al. 2007).

Figure 7 shows the radial distribution of $L(H\alpha)_{corr}$, M_{mol}^*, and $SFE_{H\alpha,24\,\mu m}$ for each cloud as a function of projected distance from the center of the main cavity in NGC 604 (01^{h}34^{m}32^s.5, +30°47′0″.5), where the central clusters are most crowded. The gradual decrease of $L(H\alpha)_{corr}$ as the radial distance increases is seen in Figure 7 (top), except for the NMA-8 region (Shell B region). However, we found a gradual increase of M_{mol}^*, which implies that star formation is active enough to consume and/or to dissipate parental clouds. We found a clear radial dependence in $SFE_{H\alpha,24\,\mu m}$; the closer to the central clusters the GMCs are located, the higher SFE they have. We should note that this is because of the combination of the radial dependence of both $L(H\alpha)_{corr}$ and M_{mol}^* rather than only of the $L(H\alpha)_{corr}$ distribution. Besides, the total flux of $L(H\alpha)_{corr}$ is considered to be contributed by both the central clusters and the young stars that might be embedded in the clouds (Section 4.1.2). As for NMA-2, NMA-6, and NMA-9, we do not know whether they are physically associated with Hα emission or not. In the case that they are observed at associations by chance, the values of SFE that we derived give just the upper limits. Nevertheless, the SFE on the bottom panel in Figure 7 still shows the tendency that SFEs decrease as the distance from the central clusters increase.

Figure 8 also shows the radial distribution of S_{HCN}/S_{CO}^* and $SFE_{89\,GHz}$ as a function of projected distance from the center of the main cavity in NGC 604. We found a radial dependence in $SFE_{89\,GHz}$, which is in good agreement with the behavior of $SFE_{H\alpha,24\,\mu m}$ (the bottom panel of Figure 7), even though these values were derived from different wavelength data. This implies that the 89 GHz continuum can be another tracer of massive-

Figure 8. $SFE_{89\,GHz}$ (top) and S_{HCN}/S^*_{CO} (bottom) distribution as a function of projected distance from the center of the main cavity in NGC 604. Its coordinate of ($01^h34^m32^s.5$, $+30°47'0''.5$) is indicated by a pink star symbol in Figure 6. The filled circles represent the detected clouds, while the open circles show the upper limit for the clouds that were not detected in HCN and 89 GHz continuum emission. The open squares represent the line ratio measured in the region where HCN emissions were detected. The distance of these two plots were measured at the peak of HCN emission. The cloud numbers are also plotted. Note that common errors are excluded in order to compare each cloud relatively.

star-forming regions. On the other hand, the radial dependence of the dense gas fraction S_{HCN}/S^*_{CO} is not clear from our data, where we have estimated upper limits. The dense gas fraction S_{HCN}/S^*_{CO} in Figure 8 (bottom) is averaged over the extent of the CO clouds (denoted as circles). However, our high-resolution images of CO and HCN emissions in Figure 4 inform us that the line ratio of S_{HCN}/S^*_{CO} shows a gradient within a single cloud because two HCN components were detected at the northern part of the CO clouds NMA-8 and NMA-9 rather than the peak of the CO emission (see Section 3.2). The line ratios of S_{HCN}/S^*_{CO} (and its locations) that were measured over the region where HCN emissions were detected are represented as an open square in the bottom panel of Figure 8. Their values are higher than the averaged value, which are represented as black circles in Figure 8, and their locations are close to the direction of the central clusters as compared with the line ratios within a single cloud. Thus, from this figure, it is found that dense gas formation has occurred at the near side of a cloud toward the central clusters.

In light of our high-resolution observational results, we reconsider the "sequential star formation" scenario in NGC 604 in more detail here than done previously (Tosaki et al. 2007). First, central clusters were formed, whose powerful stellar wind made the main cavity with Shell A; this is referred to as "first-generation star formation" in Tosaki et al. (2007). Inside Shell A, molecular gas around the central part of the stellar clusters is almost cleared out (Section 3.4; Maíz-Apellániz et al. 2004). The "remnant" cloud, i.e., NMA-4, is on the rim of Shell A. It is suggested that NMA-4 is a cloud swept up by the stellar wind from the central stellar cluster. The second-generation stars are formed in the swept-up cloud through dense gas formation and such new stars ionize the surfaces of the parental clouds.

The cloud with "dense gas and ongoing massive star formation," i.e., NMA-8, is located on the edge of Shell B, while molecular gas inside Shell B is almost cleared out. Similar to the correlation between Shell A and NMA-4, NMA-8 could have been formed with the ambient gas swept up on Shell B and compressed by stellar winds. In such a compressed dense gas on Shell B, dense gas, and stars newly formed as evidenced by

that dense gas, and star-forming regions are located at the inner wall of NMA-8 toward the central stellar cluster. Furthermore, the star-forming region in NMA-8 is much closer to the central stellar cluster than the dense gas-forming region, and hence, the central cluster, massive star-forming region, dense gas-forming region, and molecular cloud are aligned in this order. The newly born stars in NMA-8 associated with Shell B are the next generation of stars under sequential star formation, which are induced by the previous generation stars; they are "second-generation stars" as referred to by Tosaki et al. (2007), or latter generation stars.

On the other hand, the "dense gas-forming" cloud, i.e., NMA-9, is located on the edge of the extended diffuse Hα emission up to a few hundreds parsec south of the central cluster. The dense gas forming region associated with the NMA-9 cloud is located in the direction of the central stellar cluster rather than in the emission peak of the NMA-9 cloud. The expansion of the H II region into the surrounding medium can trigger star formation through dense gas formation (e.g., Elmegreen & Lada 1977). NMA-2 is located north of the diffuse Hα nebula, while NMA-9 is in the south of the nebula (Section 4.2). Their projected distances from the central stellar cluster are almost the same. If we suppose that the propagation initiated from the central stellar cluster is isotropic, dense gas is expected to be formed in NMA-2 as well as in NMA-9. NMA-9 might be compressed by the expansion of the H II region.

In summary, we explain the following scenario of sequential star formation in NGC 604. The first-generation stars (the central clusters) are formed in a GMC. The central clusters swept up the matter to form Shell A, where dense gas was formed by the compression of the cloud material. Then, second-generation stars form in the dense gas, which have already been dissipated in the parental clouds (the "remnant" cloud; NMA-4). Shell B is formed by blowout through the molecular tunnel, where another star formation occurs on the "on-going dense gas and star formation" cloud (NMA-8). At the far end beyond these shells, dense gas is formed in the quiescent molecular clouds (NMA-9) by the effect of the expansion of the H II region.

5. SUMMARY

We presented the highest sensitivity and the highest resolution ^{12}CO images of the GHR NGC 604 in the nearby galaxy M33. Moreover, we also obtained the HCN and 89 GHz continuum images. This is the first detection of HCN and 89 GHz continuum emission toward NGC 604 reported in the literature.

1. We identified ten CO molecular clouds that have sizes of 5–29 pc and masses of $(0.8–7.4) \times 10^5\ M_\odot$. They have sizes and masses comparable to the typical GMCs in our Galaxy.
2. The HCN-to-CO flux ratio of NMA-8 is 0.024 ± 0.007 and that of NMA-9 is 0.018 ± 0.007. These values are comparable to those of typical GMCs in our Galaxy and in the neighboring galaxy M31.
3. We derived the $SFE_{H\alpha,24\,\mu m}$ for each cloud from dust-corrected Hα luminosity (combination of Hα and 24 μm luminosity). We found that the $SFE_{H\alpha,24\,\mu m}$ was in good agreement with that from the 89 GHz continuum.
4. Three CO clouds show good spatial and velocity correlation with the bright Hα shells. The CO clouds show variations in SFEs, as estimated from the 89 GHz and combination of Hα and *Spitzer* 24 μm luminosity. These variations of their properties could be explained as a snapshot of molecular clouds at different evolutionary stages.

5. A clear radial dependence of SFEs from the center of the main cavity was found. Further, we found that the HCN and 89 GHz continuum emission show offset from the CO peak and are distributed in the direction of the central cluster. We interpret our results as a scenario of sequential star formation in which the massive star formation propagates through the expansion of the Hα emission nebula excited by the central OB star cluster.

REFERENCES

Bosch, G., Terlevich, E., & Terlevich, R. 2002, MNRAS, 329, 481
Brinks, E., & Bajaja, E. 1986, A&A, 169, 14
Brouillet, N., Muller, S., Herpin, F., Braine, J., & Jacq, T. 2005, A&A, 429, 153
Bruhweiler, F. C., Miskey, C. L., & Smith Neubig, M. 2003, AJ, 125, 3082
Buczilowski, U. R. 1988, A&A, 205, 29
Calzetti, D., et al. 2007, ApJ, 666, 870
Cardelli, J. A., & Clayton, G. C. 1988, AJ, 95, 516
Churchwell, E., & Goss, W. M. 1999, ApJ, 514, 188
Conti, P. S., & Blum, R. D. 2002, ApJ, 564, 827
Corbelli, E., & Salucci, P. 2000, MNRAS, 311, 441
Deharveng, L., Lefloch, B., Kurtz, S., Nadeau, D., Pomarès, M., Caplan, J., & Zavagno, A. 2008, A&A, 482, 585
Deharveng, L., Zavagno, A., & Caplan, J. 2005, A&A, 433, 565
Deul, E. R., & den Hartog, R. H. 1990, A&A, 229, 362
Diaz, A. I., Terlevich, E., Terlevich, R., Gonzalez-Delgado, R. M., Perez, E., & Garcia-Vargas, M. L. 1996, in ASP Conf. Ser. 98, From Stars to Galaxies: the Impact of Stellar Physics on Galaxy Evolution, ed. C. Leitherer, U. Fritze-von-Alvensleben, & J. Huchra (San Francisco, CA: ASP) 399
Drissen, L., Moffat, A. F. J., & Shara, M. M. 1993, AJ, 105, 1400
Elmegreen, B. G. 1998, Origins, 148, 150
Elmegreen, B. G., & Lada, C. J. 1977, ApJ, 214, 725
Engargiola, G., Plambeck, R. L., Rosolowsky, E., & Blitz, L. 2003, ApJS, 149, 343

Fariña, C., Bosch, G. L., & Barbá, R. R. 2010, in IAU Symp. 266, Star Clusters: Basic Galactic Building Blocks Throughout Time and Space, ed. R. de Grijs & J. R. D. Lépine (Cambridge: Cambridge Univ. Press), 391
Freedman, W. L., et al. 2001, ApJ, 553, 47
Fukui, Y., et al. 2008, ApJS, 178, 56
González Delgado, R. M., & Pérez, E. 2000, MNRAS, 317, 64
Heiner, J. S., Allen, R. J., & van der Kruit, P. C. 2009, ApJ, 700, 545
Helfer, T. T., & Blitz, L. 1997a, ApJ, 478, 162
Helfer, T. T., & Blitz, L. 1997b, ApJ, 478, 233
Hoopes, C. G., & Walterbos, R. A. M. 2000, ApJ, 541, 597
Hoopes, C. G., Walterbos, R. A. M., & Bothun, G. D. 2001, ApJ, 559, 878
Hunter, D. A., Baum, W. A., O'Neil, E. J., Jr., & Lynds, R. 1996, ApJ, 456, 174
Kennicutt, R. C., Jr. 1984, ApJ, 287, 116
Kennicutt, R. C., Jr., et al. 2007, ApJ, 671, 333
Maíz-Apellániz, J., Pérez, E., & Mas-Hesse, J. M. 2004, AJ, 128, 1196
Martins, F., Schaerer, D., & Hillier, D. J. 2005, A&A, 436, 1049
Mayya, Y. D. 1994, AJ, 108, 1276
Mayya, Y. D. 1995, AJ, 109, 2503
Mayya, Y. D., & Prabhu, T. P. 1996, AJ, 111, 1252
Melnick, J. 1980, A&A, 86, 304
Muraoka, K., et al. 2007, PASJ, 59, 43
Okumura, S. K., et al. 2000, PASJ, 52, 393
Rand, R. J., & Kulkarni, S. R. 1990, ApJ, 349, L43
Relaño, M., & Kennicutt, R. C. 2009, ApJ, 699, 1125
Rieke, G. H., et al. 2004, ApJS, 154, 25
Rosolowsky, E., Engargiola, G., Plambeck, R., & Blitz, L. 2003, ApJ, 599, 258
Scoville, N. Z., & Sanders, D. B. 1987, Interstellar Process., 134, 21
Scoville, N. Z., Sargent, A. I., Sanders, D. B., & Soifer, B. T. 1991, ApJ, 366, L5
Solomon, P. M., Downes, D., & Radford, S. J. E. 1992, ApJ, 387, L55
Strong, A. W., et al. 1988, A&A, 207, 1
Tenorio-Tagle, G., Muñoz-Tuñón, C., Pérez, E., Maíz-Apellániz, J., & Medina-Tanco, G. 2000, ApJ, 541, 720
Tosaki, T., Miura, R., Sawada, T., Kuno, N., Nakanishi, K., Kohno, K., Okumura, S. K., & Kawabe, R. 2007, ApJ, 664, L27
Tsutsumi, T., Morita, K.-I., & Umeyama, S. 1997, in ASP Conf. Ser. 125, Astronomical Data Analysis Software and Systems VI, ed. G. Hunt & H. E. Payne (San Francisco, CA: ASP), 50
Tüllmann, R., et al. 2008, ApJ, 685, 919
Viallefond, F., Boulanger, F., Cox, P., Lequeux, J., Perault, M., & Vogel, S. N. 1992, A&A, 265, 437
Ward-Thompson, D., & Robson, E. I. 1990, MNRAS, 244, 458
Werner, M. W., et al. 2004, ApJS, 154, 1
Whitworth, A. P., Bhattal, A. S., Chapman, S. J., Disney, M. J., & Turner, J. A. 1994, MNRAS, 268, 291
Williams, J. P., & McKee, C. F. 1997, ApJ, 476, 166
Wilson, C. D., & Scoville, N. 1990, ApJ, 363, 435
Wilson, C. D., & Scoville, N. 1992, ApJ, 385, 512
Yang, H., Chu, Y.-H., Skillman, E. D., & Terlevich, R. 1996, AJ, 112, 146
Zavagno, A., Deharveng, L., Comerón, F., Brand, J., Massi, F., Caplan, J., & Russeil, D. 2006, A&A, 446, 171